

Magnetoelastic anisotropy in Heusler-type $\text{Mn}_{2-\delta}\text{CoGa}_{1+\delta}$ films

Takahide Kubota,^{1,2, a)} Daichi Takano,¹ Yohei Kota,³ Shaktiranjan Mohanty,⁴ Keita Ito,^{1,2} Mitsuhiro Matsuki,¹ Masahiro Hayashida,¹ Mingling Sun,¹ Yukiharu Takeda,⁵ Yuji Saitoh,⁵ Subhankar Bedanta,⁴ Akio Kimura,^{6,7} and Koki Takanashi^{1,2,8}

¹⁾*Institute for Materials Research, Tohoku University, Sendai 980-8577, Japan*

²⁾*Center for Spintronics Research Network, Tohoku University, Sendai 980-8577, Japan*

³⁾*National Institute of Technology, Fukushima College, Iwaki, Fukushima 970-8034, Japan*

⁴⁾*Laboratory for Nanomagnetism and Magnetic Materials (LNMM), School of Physical Sciences, National Institute of Science Education and Research, HBNI, Jatni 752050, Odisha, India*

⁵⁾*Materials Sciences Research Center, Japan Atomic Energy Agency, Hyogo 679-5148, Japan*

⁶⁾*Graduate School of Science, Hiroshima University, Higashi-hiroshima 739-8526, Japan*

⁷⁾*Graduate School of Advanced Science and Engineering, Hiroshima University, Higashi-hiroshima 739-8526, Japan*

⁸⁾*Center for Science and Innovation in Spintronics (Core Research Cluster), Tohoku University, Sendai 980-8577, Japan*

(Dated: 27 August 2021)

Perpendicular magnetization is essential for high-density memory application using magnetic materials. High-spin polarization of conduction electrons is also required for realizing large electric signals from spin-dependent transport phenomena. Heusler alloy is a well-known material class showing the half-metallic electronic structure. However, its cubic lattice nature favors in-plane magnetization and thus minimizes the perpendicular magnetic anisotropy (PMA), in general. This study focuses on an inverse-type Heusler alloy, $\text{Mn}_{2-\delta}\text{CoGa}_{1+\delta}$ (MCG) with a small off-stoichiometry (δ), which is expected to be a half-metallic material. We observed relatively large uniaxial magnetocrystalline anisotropy energy (K_u) of the order of 10^5 J/m³ at room temperature in MCG films with a small tetragonal distortion of a few percent. A positive correlation was confirmed between the c/a ratio of lattice constants and K_u . Imaging of magnetic domains using Kerr microscopy clearly demonstrated a change in the domain patterns along with K_u . X-ray magnetic circular dichroism (XMCD) was employed using synchrotron radiation soft x-ray beam to get insight into the origin for PMA. Negligible angular variation of orbital magnetic moment (Δm_{orb}) evaluated using the XMCD spectra suggested a minor role of the so-called Bruno's term to K_u . Our first principles calculation reasonably explained the small Δm_{orb} and the positive correlation between the c/a ratio and K_u . The origin of the magnetocrystalline anisotropy was discussed based on the second-order perturbation theory in terms of the spin-orbit coupling, claiming that the mixing of the occupied \uparrow - and the unoccupied \downarrow -spin states is responsible for the PMA of the MCG films.

^{a)}takahide.kubota@tohoku.ac.jp; author to whom correspondence should be addressed.

I. INTRODUCTION

Heusler alloys have been attracting interests because of its various physical properties with selection of a plenty of compositions.¹ Especially, in spintronics research field, half-metallic electronic structure, providing fully spin-polarized conduction electrons, has motivated spin-dependent transport studies such as magnetoresistance effects. Among several kinds of Heusler alloys, Co-based Heusler alloys, *e.g.* Co_2YZ , Y : a transition metal, Z : a 12 or 13 group element, are representative materials that have been predicted to show the half-metallicity.²⁻⁶ The half-metallicity was experimentally deduced from the large magnetoresistance effects,⁷⁻¹⁴ the X-ray absorption spectroscopy¹⁵⁻¹⁸ and photoelectron spectroscopy.^{19,20} Recent bulk-sensitive angle-resolved photoelectron spectroscopy experiments of Co_2MnGe with soft X-ray synchrotron radiation beam uncovered three-dimensional energy dispersions, which are in good agreement with the theoretical band structures.¹⁸ In contrast to Co-based Heusler alloys, Mn-based Heusler alloys, Mn_2YZ gained renewed interests as a new class of half-metallic Heusler alloys.^{4,21} The major advantage of the Mn-based Heusler alloy is relatively small saturation magnetization (M_s) which reduces critical current density for current induced magnetization switching phenomena based on spin-transfer-torque (STT).²² In addition, some of the Mn-based Heusler alloys with the inverse-Heusler structure (X_A phase) were predicted to possess novel electronic structures, *e.g.* half-metallic spin-gapless semiconductor.²³⁻²⁵ Among the Mn-based Heusler alloys, Mn_2CoGa is highlighted in this paper. The Mn_2CoGa is a theoretically predicted half-metallic inverse-type Heusler alloy.²⁶⁻²⁸ The composition dependent magnetocrystalline anisotropy is an interesting feature in the Mn_2CoGa and the related compositions: Tetragonal distortion of the lattice occurs due to the band Jahn-Teller effect in $\text{Mn}_{3-x}\text{Co}_x\text{Ga}$ alloys with x below 0.5, and relatively large magnetocrystalline anisotropy of the order of 10^6 J/m³ has been observed.^{26,29,30} The tetragonal distortion destroys the half-metallic energy gap, while the conduction electron maintains relatively high spin polarization due to the difference in the electron mobilities between the majority and minority spin channels.²⁸ Recent studies also reported another interesting property of a Mn_2CoGa film showing perpendicular magnetic anisotropy (PMA) originating from the magnetocrystalline anisotropy in a nearly cubic lattice.³¹ In the previous study, $\text{Mn}_{2-\delta}\text{CoGa}_{1+\delta}$ (MCG) films ($\delta \sim 0.1$) grown onto a MgO (001) single crystal substrate exhibited perpendicular magnetization and in-plane magnetization with and without a Cr buffer layer underneath, respectively. Such a drastic change can be ascribed to a small

difference in the lattice strain, c/a ratios which were 1.00 and 1.01 for the films without and with the Cr buffer layer, respectively. The previous results suggested that the small lattice strain induced magnetocrystalline anisotropy in MCG in the cubic phase, *i.e.*, the magnetoelastic anisotropy was induced, which is totally different from the interface PMA in Co-based full-Heusler alloys containing Fe, for which PMA energy of the order of 10^5 J/m³ was reported in ultra-thin, ~ 1 nm, films layered with MgO.^{32–35} The PMA in highly spin polarized materials is essential for spintronic devices, such as STT-type magnetoresistive random access memories. Concerning the MCG, however, the half-metallicity in the strained lattice as well as the origin of the magnetocrystalline anisotropy remains unsolved thus far.

In this study, a set of MCG epitaxially grown films showing different PMA and c/a ratios were prepared, and correlations between the magnetic properties, magnetic domain images, and electronic structures were discussed based on experimental results and theoretically calculated electronic structures. To figure out the chemical order and electronic structures of film samples, synchrotron radiation soft x-ray absorption spectra (XAS) and soft x-ray magnetic circular dichroism (XMCD) were also investigated. There were many reports with XAS and XMCD results on Heusler alloys containing Mn atoms^{15,16,36} including Mn₂CoGa.^{27,37,38} In the previous studies, the degree of the electron localization was discussed using the XAS and XMCD spectra, which are also addressed in this study.

II. EXPERIMENTAL PROCEDURES

All samples were deposited onto MgO(001) single-crystal substrates by using an ultrahigh-vacuum magnetron sputtering machine with a base pressure below 3×10^{-7} Pa. The MCG layers were prepared by co-sputtering technique using a Mn₅₅Ga₄₅ target and a Co target. The film composition of the MCG layer was Mn_{42.6}Co_{24.3}Ga_{33.1} (at.%) corresponding to Mn_{1.7}CoGa_{1.3} in the atomic ratio, which was characterized by an electron probe micro analyzer with a standard sample for the quantitative analysis. We employed two materials for the buffer layer dependence study: Ag and Cr. The stacking structures of samples and the name for the sample series were as follows: Series A (Ag buffer): MgO sub. /Cr (20 nm) /Ag (40 nm) / MCG (t) /Ta (3 nm), and series B (Cr buffer): MgO sub. /Cr (20 nm) / MCG (t) /Ta (3 nm). The thicknesses (t) of the MCG layer were 5, 10, 20 and 30 nm. Before installing the samples inside the vacuum chamber, the substrates were cleaned using

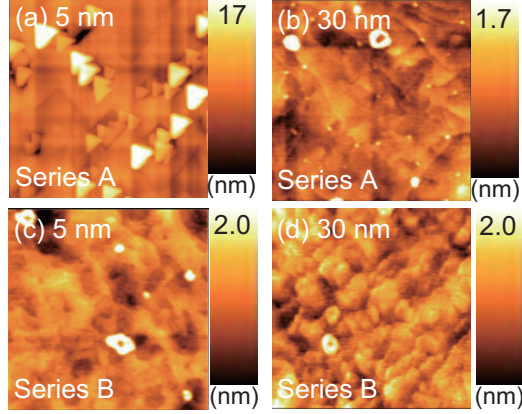


FIG. 1. Atomic force microscope images of the sample surfaces. Series A: (a) t : 5, and (b) 30 nm. Series B: (c) t : 5, and (d) 30 nm. Scan-area is $1 \times 1 \mu\text{m}^2$ for all the images.

acetone and ethyl alcohol, and after introducing them inside the chamber, the substrates were annealed at $700 \text{ }^\circ\text{C}$ to clean the surface. All layers were deposited at room temperature, and *in situ* post-annealing was carried out at $700 \text{ }^\circ\text{C}$ ($500 \text{ }^\circ\text{C}$) for the Cr (MCG) layer. The morphology of the sample surfaces was observed by using an atomic force microscope (AFM) after depositing a Ta capping layer. The crystal structures and magnetic properties were characterized by x-ray diffraction (XRD), and using a vibrating sample magnetometer (VSM), respectively, at room temperature.

The hysteresis loop and domain images were recorded simultaneously by magneto-optical Kerr effect (MOKE) microscopy manufactured by Evico Magnetics Ltd. Germany. All the samples were measured in polar MOKE (P-MOKE) geometries in which the sample surface was perpendicular to the applied magnetic field.

The XAS and XMCD measurements were carried out on $L_{2,3}$ -edges of Mn and Co atoms by a total electron-yield method at the twin helical undulator beamline BL23SU of SPring-8.³⁹ External magnetic fields (H) of $\pm 3 \text{ T}$ and $\pm 8 \text{ T}$ were applied for measurements at out-of-plane field (θ : 0°) and pseudo in-plane field (θ : 54.7°), respectively. The measurement temperature was set at 300 K .

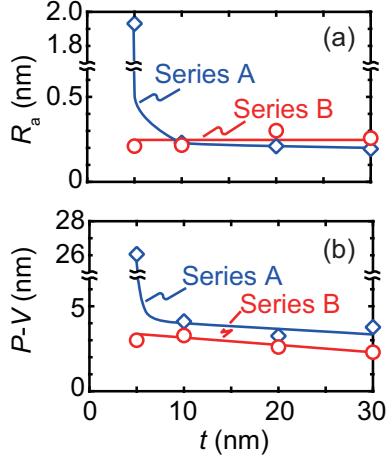


FIG. 2. Summary of (a) average surface roughness (R_a) and (b) peak-to-valley height ($P-V$) values as a function of t .

III. RESULTS AND DISCUSSION

A. Surface Morphology and Crystal Structure

Surface morphologies were observed using AFM and the results are shown in figures 1(a)–1(d) for the series A and B with t of 5 and 30 nm. For the 5-nm-thick samples, several islands with a height of several nanometers are observed in series A (Fig. 1(a)), while relatively flat surface is observed in series B (Fig. 1(c)). Regarding the 30-nm-thick samples, the surfaces are relatively flat for both series A and B. The thickness dependence of the average surface roughness (R_a) and peak-to-valley height ($P-V$) are summarized in figures. 2(a) and 2(b), respectively. The values of R_a and $P-V$ drastically drop at $t = 10$ nm for series A, while, those values show no dependence on t and relatively small values for series B. These results suggest a difference in the growth mode of the MCG layers depending on the buffer material: For the series A using Ag buffer layer, the Volmer-Weber (VW) mode, which describes a three-dimensional growth, is considered for the initial growth of the MCG layer. It then possibly changes to the Frank-van-der-Merwe (FM) mode for a layer-by-layer growth mode with increasing t . For the series B using Cr buffer layer, the film was grown possibly in the FM mode throughout the whole thicknesses. The lattice spacings of both buffer materials are smaller than that of a bulk Mn_2CoGa ,²⁶ and the lattice mismatches are approximately 1.6% and 1.4% to the Cr and Ag buffer layers, respectively, which are of the same order. A reason for the difference in the growth modes between the two sample series can be qualitatively

TABLE I. Reported surface energies in literature.

Refs.	Surface energy (J/m ²)		
	45 ^a	46 ^b	47 ^c
Cr	2.056	2.300	3.979
Ag	1.302	1.250	1.200

^a Thermodynamic calculation for poly-crystalline system.

^b Experimental value for poly-crystalline samples.

^c Calculated values for (001) surface based on full-charge density linear muffing-tin orbitals method.

understood by considering surface energies for the buffer/MCG layer system in the following way: According to the quasi-equilibrium description, a sum of surface energies (σ_{sum}) can be written as $\sigma_{\text{sum}} = \sigma_f - \sigma_b + \sigma_i$, where σ_f , σ_b , and σ_i are surface energies of a film, a buffer layer, and the interface energy between the film and the buffer layer, respectively.^{40,41} Here, strain energies for the film and the buffer layer are neglected because the lattice strain is small (\sim a few %) in the present samples. We may also neglect the difference between σ_i values for the cases of series A (Ag/MCG interface) and series B (Cr/MCG interface), because the σ_i depends on the lattice misfits between the layers which are comparable to each other for the present sample series. In addition, contribution of σ_i to the value of σ_{sum} could be very small because the potential energy for the interface energy exhibits exponential decrease when the misfit is close to zero.⁴²⁻⁴⁴ Based on the points stated above, σ_f and σ_b can be dominant parameters affecting the sign of $\sigma_{\text{sum}} \sim \sigma_f - \sigma_b$, *i.e.* VW (FM) mode is expected for $\sigma_{\text{sum}} > 0$ (< 0) for which σ_f is larger (smaller) than σ_b .

Reported surface energies for poly-crystalline and (001) surface of the cubic systems are summarized in Table I.⁴⁵⁻⁴⁷ Although the surface energy of MCG is unknown here, we may qualitatively understand the different growth modes considering the surface energies of Cr and Ag as σ_b , *i.e.*, the surface energies of Cr are larger than those of Ag for all the cases shown in Table I. Thus, the σ_{sum} can be relatively small for the Cr buffer sample compared to that using the Ag buffer sample, which possibly resulted in better coverage of the MCG layer deposited on the Cr buffer than that on the Ag buffer.

The out-of-plane and in-plane XRD measurements were carried out to investigate the crystal structure. The XRD profiles of 5-nm-thick samples are shown in figure 3 for series

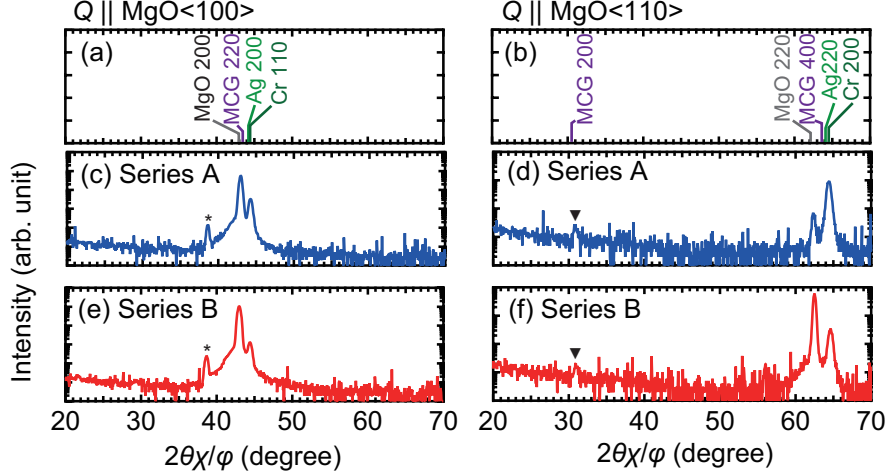


FIG. 3. In-plane XRD profiles of 5-nm-thick samples. (a, b) Diffraction positions for MCG, Ag, Cr layers, and MgO substrates. (c, d) Diffraction profiles of series A, and (e, f) those of series B. Diffraction vectors (\vec{Q}) are parallel to MgO< 100 > and MgO< 110 > for (c, e) and (d, f), respectively.

A (Figs. 3(c) and 3(d)) and B (Figs. 3(e) and 3(f)). From the MCG layer, a series of $h\ 0\ 0$ ($h = 2$ or 4) diffractions are observed for the diffraction profile with $\vec{Q}||\text{MgO}[110]$, and only $2\ 2\ 0$ diffractions are observed for $\vec{Q}||\text{MgO}[100]$ where \vec{Q} is a diffraction vector. Features of these diffraction profiles were similar for all other samples indicating the epitaxial growth with a relationship of $\text{MgO}(001)[100] \parallel \text{MCG}(001)[110]$. Figures 4(a), 4(b), and 4(c) show the t dependence of the out-of-plane lattice constant (c), the in-plane lattice constants (a), and the c/a ratio, respectively. For the series A, the c/a ratio shows nearly no dependence on t , on the other hand for the series B, although the c/a ratio is 1.04 at $t = 5$ nm and relaxes with increasing t , the tetragonal distortion is maintained at a relatively thick t of 30 nm for which the c/a ratio is 1.02. The different lattice strain possibly originates from the difference in the growth modes of the MCG layers: For the series A, as it was found in the observation of morphology using the AFM images, the strain inside the lattice could be relaxed because of the three-dimensional growth mode in the initial stage. For the series B, on the other hand, the layer-by-layer growth in the initial stage resulted in the restriction of the MCG lattice to the in-plane direction, which remained unrelaxed even at the relatively large thickness.

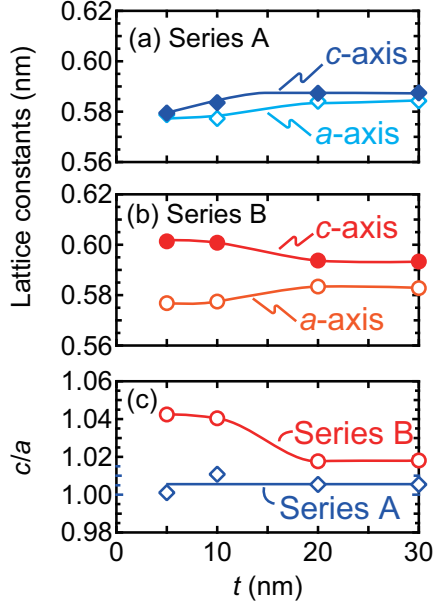


FIG. 4. Thickness (t) dependence of lattice constants of the samples: (a) series A on Ag buffers, (b) series B on Cr buffers, and (c) the t dependence of c/a ratios for series A and B.

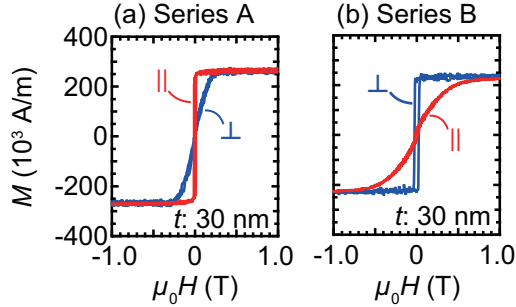


FIG. 5. Magnetization curves for 30-nm-thick samples of (a) series A and (b) B. Marks \perp and \parallel represent the out-of-plane and in-plane directions, respectively, for applied magnetic fields.

B. Magnetic Properties

Figure 5 shows magnetization curves of 30-nm-thick samples for the series A and B. In-plane magnetization is observed for the series A, and perpendicular magnetization is observed for the series B. The perpendicular magnetization in series B is consistent with a previous study on a $\text{Mn}_{1.8}\text{Co}_{1.2}\text{Ga}_{1.0}$ film.³¹ These features for the easy magnetization directions were the same for all other layer thicknesses down to 5 nm in each sample series. Magnetization curves for all samples are shown in Supplementary Material. Figure 6(a) shows the t dependence of saturation magnetic moments (μ_s) which were calculated using

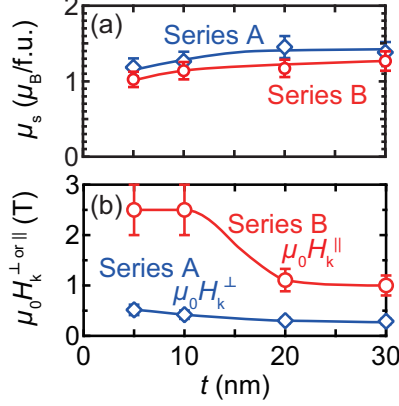


FIG. 6. (a) Saturation magnetic moment (μ_s) per a formula unit (f.u.) and (b) saturation field ($H_k^{\perp(\text{or } \parallel)}$) as a function of t , where $H_k^{\perp(\text{or } \parallel)}$ represents anisotropy field for out-of-plane (in-plane) direction.

M_s values obtained from the magnetization curves and the lattice constants (Fig. 4). The μ_s shows nearly no dependence on t . The magnitudes of μ_s range from 1.1 to 1.4 μ_B per a formula unit (f.u.), which are relatively small compared to other ferromagnetic Heusler alloys showing the moment of the order of 4 – 6 μ_B because of the ferrimagnetic alignment of the atomic moments. Although the experimental values are smaller than theoretical values of approximately 2 μ_B for Mn_2CoGa in literature⁴⁸ as well as in our calculation (see Sec. IV), those are of the same order of other calculated values of about 1 μ_B in which the off-stoichiometry and the disorder effects were considered.⁴⁹ Comparing the two sample series, the samples in series A exhibit slightly larger μ_s than those in series B. The difference is possibly because of a small difference of chemical order for each sample series. Figure 6(b) shows the t dependence of saturation field for hard magnetization directions which are the out-of-plane field (H_k^{\perp}) and the in-plane field (H_k^{\parallel}) for series A and B, respectively. The H_k^{\perp} monotonically decreases as t increases for the series A, while H_k^{\parallel} shows a drop around the t of greater than 10 nm for the series B. The uniaxial magnetocrystalline anisotropy energy (K_u) of MCG films was evaluated from the magnetization curves using the following formula; $K_u = K_u^{\text{eff}} + (\mu_0/2)M_s^2$, where $(\mu_0/2)M_s^2$ is the shape anisotropy energy, and K_u^{eff} was derived from the area enclosed by the out-of-plane and in-plane magnetization curves. A positive value of K_u^{eff} represents the perpendicular magnetization in this study. The values of K_u are summarized as a function of the c/a ratios in figure 7. Here, the K_u exhibits positive correlation with the c/a ratio indicating that it is caused by the magnetoelastic effect. The maximum value of K_u was 1.6×10^5 J/m³ at the c/a of 1.04.

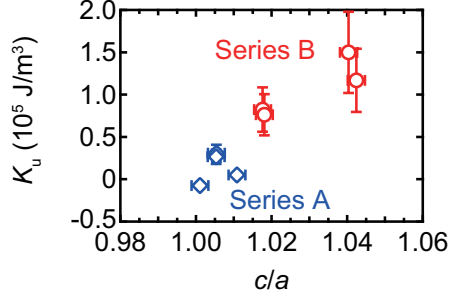


FIG. 7. The c/a ratio dependence of uniaxial magnetocrystalline anisotropy energy, K_u .

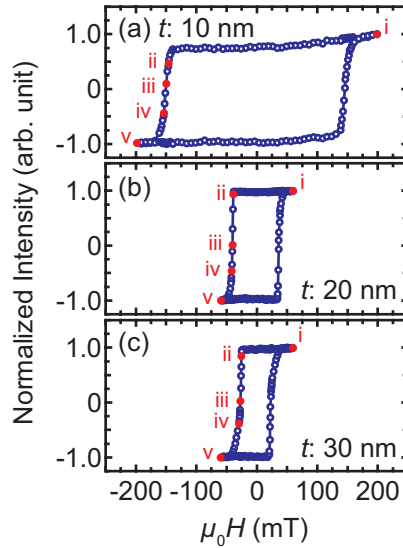


FIG. 8. The hysteresis loops for $t =$ (a) 10, (b) 20, and (c) 30 nm in series B measured with Kerr microscopy in polar mode. The red dots and numbers i – v on the hysteresis loops corresponds to the points for which domain images are shown in the next figure *i.e.*, Fig. 9.

C. Domain Observations

The values of K_u exhibit clear dependence on t , especially in the samples of series B, for which the difference in magnetic domain structures was also observed using Kerr microscopy.^{50,51} Figure 8 shows hysteresis loops for the samples of series B with $t =$ 10 (Fig. 8(a)), 20 (Fig. 8(b)) and 30 nm (Fig. 8(c)) measured by MOKE in polar mode. The square like shapes of the hysteresis indicate that the magnetization reversal occurs via domain nucleation and domain wall motion for all the samples.^{50,52} To clarify the change of domain pattern, five points were chosen for MOKE microscopy observation: (i) a saturation point at a positive field ($+H_{\text{sat}}$), (ii) a point around nucleation at a negative field ($-H_{\text{nuc}}$), (iii) a point around coercivity at a negative field ($-H_c$), (iv) a point near saturation in a

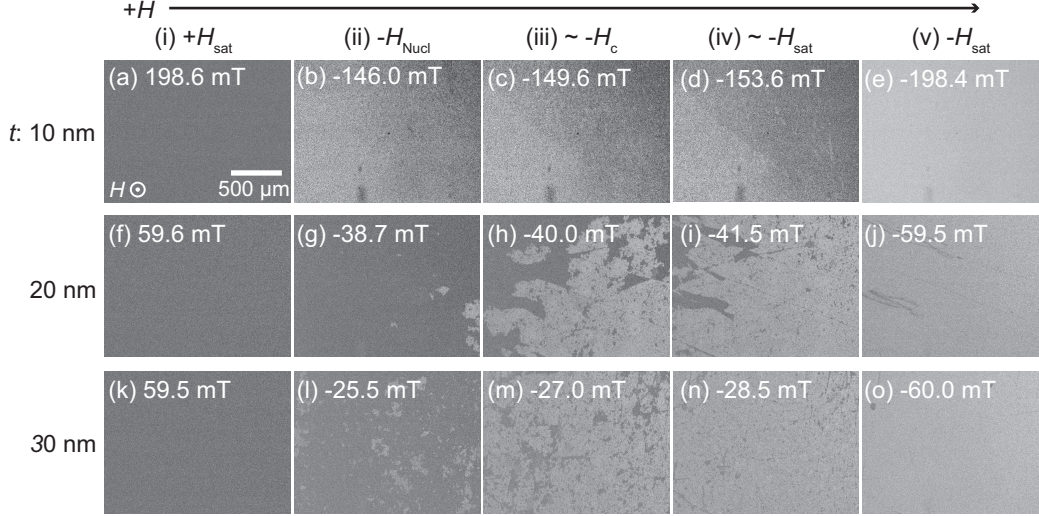


FIG. 9. The domain images for (a – e) $t = 10$, (f – j) 20, and (k – o) 30 nm in series B, whose hysteresis loops are shown in Figs. 8(a), 8(b), and 8(c), respectively. The field points (i – v) which are shown above the panels are annotated in Fig. 8. The exact field values are shown in each panel. The scale bar and field direction are shown in (a), which is valid for all the images.

negative field ($\sim -H_{\text{sat}}$), and (v) a saturation point for the negative field ($-H_{\text{sat}}$). The numbers, i – v are also annotated in each panel of Fig. 8, and the respective field values are shown in each panel of MOKE images in Fig. 9. The domain images observed by MOKE microscopy in polar mode of three samples are shown in figure 9. Note that the domain image was not studied for $t = 5$ nm because of large H_c (~ 210 mT) which was out of the range of the MOKE setup. For the 10-nm-thick sample, relatively large size of domains appears, which contain a 180° domain wall and are visible in Figs. 9(b) to 9(d). The domain pattern changes for $t = 20$ nm, in which large patch-like domains are observed (Figs. 9(g) – 9(i)). With increasing t to 30 nm, the domain size becomes small (Figs. 9(l) – 9(n)). It is observed here that the domain size is observed to be comparatively large for the sample with large anisotropy energy.

D. X-ray Magnetic Circular Dichroism

Element specific magnetic moment of the 30-nm-thick sample showing perpendicular magnetization (series B) was characterized using synchrotron radiation soft x-ray at BL23SU of SPring-8.³⁹ The XAS ($= \mu^- + \mu^+$) and XMCD ($= \mu^- - \mu^+$) spectra are shown in figure 10 for Mn $L_{2,3}$ and Co $L_{2,3}$ absorption edges measured at θ of 0° and 54.7° , where $\mu^{+(-)}$ represents

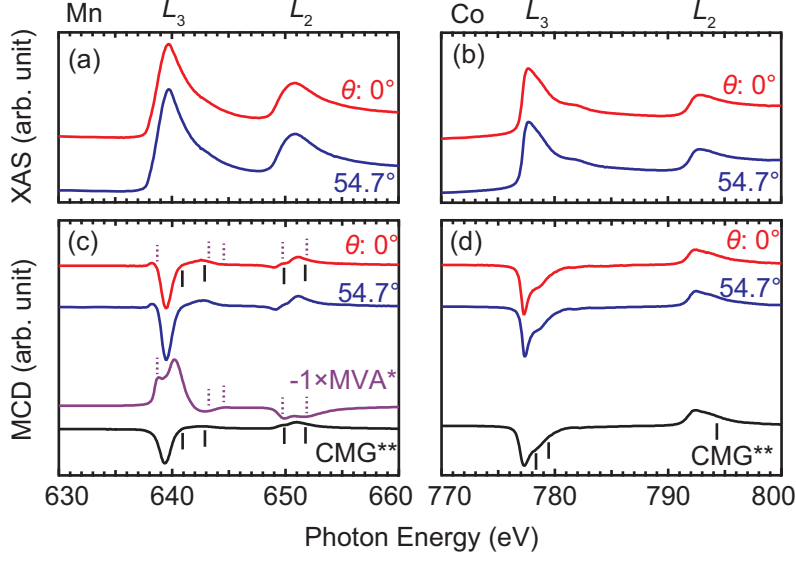


FIG. 10. (a, b) Normalized soft x-ray absorption spectra (XAS) and (c, d) soft x-ray magnetic circular dichroism (XMCD) spectra for the series B sample around the (a, c) Mn $L_{2,3}$ and (b, d) Co $L_{2,3}$ absorption edges. Red lines and blue lines represent spectra taken at $\theta = 0^\circ$ and 54.7° , respectively, where $\theta = 0^\circ$ is the perpendicular to the film plane direction. MVA and CMG are reference spectra of bulk Mn_2VAI ³⁶ and Co_2MnGa ¹⁷ samples, respectively. Positions for the shoulders in XMCD spectra are marked by dotted lines and solid lines for those in MVA and CMG, respectively, and the corresponding structures are also marked in the spectra of series B sample using the same markers.

the soft x-ray absorption for the positive (negative) helicity. The XAS and XMCD spectra of previously studied bulk Mn_2VAI ³⁶ and Co_2MnGa ¹⁷ samples are also shown in Fig. 10 to discuss the origin of structures observed in the spectra for the series B sample, which is to be described in the latter part of this section. To quantitatively discuss the angular dependence of XMCD, orbital- (m_{orb}^θ) and effective spin-moments ($m_{\text{spin}}^{\text{eff}}$) per an atom were evaluated using magneto-optical sum rules^{53–58} which state the moments using the following equations;

$$m_{\text{orb}}^\theta = -\frac{4q}{3r}n_h, \quad (1)$$

$$m_{\text{spin}}^{\text{eff}} = m_{\text{spin}} + 7m_T^\theta = -\frac{6p - 4q}{r}Cn_h, \quad (2)$$

where m_{spin} and m_T^θ are the spin-moment and magnetic dipole moment, respectively. The quantities, p , q , and r are the XMCD integrations for the L_3 -edge, $L_3 + L_2$ -edges, and

the integral of XAS which are defined as the following equations: $p = \int_{L_3}(\mu^- - \mu^+)dE$, $q = \int_{L_3+L_2}(\mu^- - \mu^+)dE$, and $r = \int_{L_3+L_2}(\mu^- + \mu^+ - \text{b.g})dE$ (b.g is a background spectrum showing a step-function shape). A correction factor (C) is included in equation (2) to take into account the so-called jj mixing effect.^{59–61} For $m_{\text{spin}}^{\text{eff}}$ of Mn and Co, the C of 1.5 and 1.1 were assumed, respectively.^{36,59,60} The numbers of 3d holes (n_h) were assumed to be 4.44 ± 0.08 and 2.29 ± 0.02 for the Mn and Co atoms, respectively, based on the theoretical values for Mn_2CoGa obtained from the first principles calculations in section IV.⁶² The values of $m_{\text{spin}}^{\text{eff}}$, m_{orb}^θ and $m_{\text{orb}}/m_{\text{spin}}^{\text{eff}}$ are summarized in figure 11. Corresponding total magnetic moment was calculated to be $1.18 \pm 0.03 \mu_B/\text{f.u.}$ using $m_{\text{spin}}^{\text{eff}}$ and m_{orb}^θ at $\theta = 54.7^\circ$, and the film composition. The total magnetic moment by the sum rule is of the same order as the μ_s of $1.27 \mu_B/\text{f.u.}$ measured by VSM. Concerning the angular dependence, no θ dependence was found either for $m_{\text{spin}}^{\text{eff}}$ or m_{orb}^θ . Here, the θ of 54.7° is a magic angle for which $m_T^\theta = 0$ by applying the approximate symmetry relation of $2m_T^{90^\circ} + m_T^{0^\circ} = 0$, where $m_T^\theta = m_T^{90^\circ} \sin^2 \theta + m_T^{0^\circ} \cos^2 \theta$ for 3d metals.^{55,63} Thus, the angular independent $m_{\text{spin}}^{\text{eff}}$ values suggest that the magnetic dipole moment is negligibly small in the present sample. The angular independent m_{orb}^θ values provide information for the discussion of origin of PMA in series B: The magnetocrystalline anisotropy energy (E_{MCA}) has been theoretically evaluated using expressions based on the second-order perturbation theory in terms of spin-orbit interactions.^{64–66} Within a formulation by Bruno, E_{MCA} can be expressed as follows:⁶⁴

$$E_{\text{MCA}} = \frac{\xi}{4} \Delta m_{\text{orb}}, \quad (3)$$

where ξ and Δm_{orb} are the spin-orbit coupling constant and the anisotropy of orbital magnetic moment defined as $\Delta m_{\text{orb}} = m_{\text{orb}}^{\theta=0} - m_{\text{orb}}^{\theta=90^\circ}$, respectively, for which only the spin-conservation terms are considered in virtual excitations contributing to the energy difference. The experimentally observed angular independent m_{orb}^θ implies small contribution of the spin-conservation terms to K_u , and the other contribution of the spin-flip terms discussed in refs. 65 and 66 is more important. Theoretical values of K_u and m_{orb} as well as the origin of PMA are to be discussed further in section IV.

The sub-peaks and shoulder structures in XAS and XMCD spectra provide additional information on the chemical order of the atoms in Heusler structures.^{15–17,27,36–38,67,68} Figure 12 shows a schematic illustration of a crystal structure for Heusler alloys and the notations of the atomic sites for the inverse-Heusler structure (X_A phase), the full-Heusler structure ($L2_1$ phase), and an $L2_{1b}$ phase. In addition to these three phases, fully-disordered $D0_3$ phase was

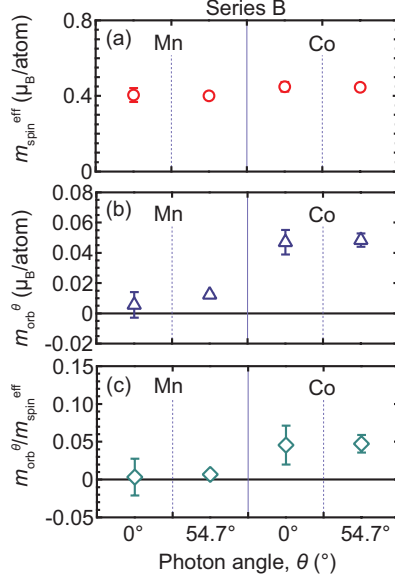


FIG. 11. Summary of (a) the effective spin-moment ($m_{\text{spin}}^{\text{eff}}$) and (b) orbital moment (m_{orb}^{θ}) per a atom evaluated using magneto-optical sum rule. (c) $m_{\text{orb}}^{\theta}/m_{\text{spin}}^{\text{eff}}$ values. Photon angles, $\theta = 0^\circ$ and 54.7° are defined as the out-of-plane and pseudo-in-plane directions, respectively. All data points are for the series B sample.

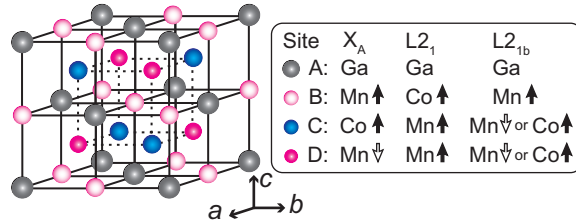


FIG. 12. Schematic illustration of the Heusler structure, and possible atomic sites for Mn_2CoGa . Relative directions of magnetic moments for each atom theoretically reported in ref. 48 are described using black and white arrows beside the name of atoms.

considered as possible chemical phases in previous studies on bulk samples.^{48,69} According to total energy calculations in ref. 48, the X_A phase was the most stable at the ground state, and relatively small energy difference of 0.136 eV/f.u. was reported for the $L2_{1b}$ phase. The energy differences with respect to the X_A phase were much higher for the $L2_1$ and $D0_3$ phases than that for the $L2_{1b}$ phase. Concerning the magnitudes of magnetic moment for each atom, the values were similar in X_A and $L2_{1b}$ phases to each other and ferrimagnetic coupling was reported as schematically shown in Fig. 12, which resulted in a total moment of about $2.0 \mu_B/\text{f.u.}$ for both. On the other hand, those were relatively large (small) for the $L2_1$

(D0₃) phase showing ferromagnetic (ferrimagnetic) coupling with a total moment of about 7.7 (1.0) μ_B /f.u. As it was discussed on Fig. 6 in Sec. III B, the total magnetic moments of the present samples are of the order of the reported values for the X_A and L2_{1b} phases, and considering the calculated energy difference mentioned above, the L2₁ and D0₃ phases are excluded in the following discussion. Note that the L2_{1b} phase was experimentally proposed for the previous bulk Mn₂CoGa samples based on high-angle annular dark field scanning electron transmission microscope images⁶⁹ and neutron diffraction experiments.⁴⁸ On the other hand, the X_A phase was proposed in another previous study on an epitaxially grown Mn₂CoGa film based on XAS and XMCD results.³⁷ The shapes of XAS and XMCD spectra of Mn₂CoGa films were previously discussed based on the first-principles calculation for the X_A phase. In the previous studies^{37,38}, several shoulders, sub-peaks, and dip structures were mentioned. In the present results, similar structures are observed, *i.e.*, broad shoulders in the XAS, and sub-peaks and dip structures in the XMCD spectra are observed, which are marked by solid and broken lines in Fig. 10. The marked structures in the XMCD spectra can also be understood as a sum of two spectra^{27,37,38,68} which are, *e.g.*, MVA³⁶ and CMG¹⁷ for the markers of broken and solid lines, respectively. Here, MVA is a typical example of a material with Mn atom(s) at D(C)-site, and CMG is another example with a Mn atom at B-site in Fig. 12. The broad feature is mainly from the Mn atom(s) D(C)-site showing relatively itinerant nature of electrons³⁶, on the other hand, the Mn atom at the B-site exhibits relatively localized nature showing remarkable shoulders in XAS.¹⁵⁻¹⁷ Concerning the XMCD spectra for Co, shoulders are also observed around the post-absorption edges with the solid markers in Fig. 10(d) which also includes a reference spectrum of CMG. The origin of the shoulders is attributed to the 2p \rightarrow 3d e_g (or e_u) transition.¹⁷

IV. FIRST-PRINCIPLES CALCULATION

First-principles calculation of electronic structure and magnetic properties of Mn₂CoGa with the X_A and L2_{1b} phases were performed by employing the tight-binding linear muffin-tin orbital method under the local spin-density functional approximation.⁷⁰ The coherent potential approximation was adopted to treat the partial disorder between Mn and Co in C- and D-sublattices of the L2_{1b} phase (see Fig. 12). We have confirmed that the electronic structure is half-metallic in both phases and the calculated magnetization is close to integer 2 μ_B /f.u., which is consistent with a previous calculation by Umetsu, Tsujikawa *et al.*⁴⁸

For the calculation of K_u and m_{orb} , spin-orbit interaction was taken into account.⁷¹ The K_u value was evaluated from the energy difference between when the magnetization aligned along the c - and a -axis directions, *i.e.*, $K_u = (E_a - E_c)/V$,^{72,73} within the magnetic force theorem (V : volume of a unit cell). The number of k-point sampling was set to 55,440 in the full-Brillouin zone.

Figure 13 shows the calculated result of K_u of Mn_2CoGa in the X_A and $L2_{1b}$ phases as a function of the axial ratio c/a , where c/a was changed under the assumption of constant volume deformation. PMA appears for $c/a > 1$ in both phases. The K_u values at $c/a = 1.04$ in the X_A and $L2_{1b}$ phases are $1.5 \times 10^5 \text{ J/m}^3$ (0.049 meV/f.u.) and $2.6 \times 10^5 \text{ J/m}^3$ (0.081 meV/f.u.), respectively, which are quantitatively consistent values with the obtained experimental result shown in Fig. 7. Figure 14 shows the m_{orb} of Mn and Co atoms when the relative angle between magnetization and crystal c -axis is 0° , 54.7° , and 90° for $c/a = 1.04$. Note that the positive (negative) sign of m_{orb} means that the direction of orbital magnetic moment and overall magnetization are the same (opposite). Thus, the directions of spin and orbital magnetic moments are the same each other in Mn at D-sublattice with X_A phase and in Mn at C/D-sublattice with the $L2_{1b}$ phase, because the spin magnetic moment is arranged in the opposite direction with the magnetization. This result is in agreement with a previous first-principles calculation.³⁷ In Fig. 14, we find that the Δm_{orb} is of the order of $0.001 \mu_B/\text{atom}$ in Co and even smaller in Mn. Based on Eq. (3), therefore, the orbital moment anisotropy cannot explain the magnetocrystalline anisotropy observed in our experiment. This fact implies that the PMA in Mn_2CoGa is mainly induced by the hybridization of \uparrow -spin and \downarrow -spin states via spin-orbit coupling, which is similar to PMA in $\text{Mn}_{3-\delta}\text{Ga}$ alloys.⁷⁴

For a detailed analysis of magnetocrystalline anisotropy, we introduce the expression of K_u based on the second-order perturbation theory in terms of the spin-orbit coupling,

$$K_u = \frac{\xi^2}{4V} \sum_{\sigma\sigma'} \sum_{u\sigma'} \frac{2\delta_{\sigma,\sigma'} - 1}{\varepsilon_{u\sigma'} - \varepsilon_{\sigma\sigma}} [|\langle u^{\sigma'} | \ell_z | o^\sigma \rangle|^2 - |\langle u^{\sigma'} | \ell_x | o^\sigma \rangle|^2], \quad (4)$$

where $\varepsilon_{\sigma\sigma}$ and $|o^\sigma\rangle$ ($\varepsilon_{u\sigma}$ and $|u^\sigma\rangle$) denote the eigenvalue and eigenvector of the nonperturbative occupied (unoccupied) states, respectively ($\sigma = \uparrow$ or \downarrow). In addition, ℓ_z (ℓ_x) is the z (x) component of the orbital angular momentum operator. From the sublattice decomposition analysis of magnetocrystalline anisotropy energy^{75,76}, we confirmed that Mn and Co in C- and/or D-sublattice mainly yields the PMA in tetragonally distorted Mn_2CoGa for $c/a > 1$

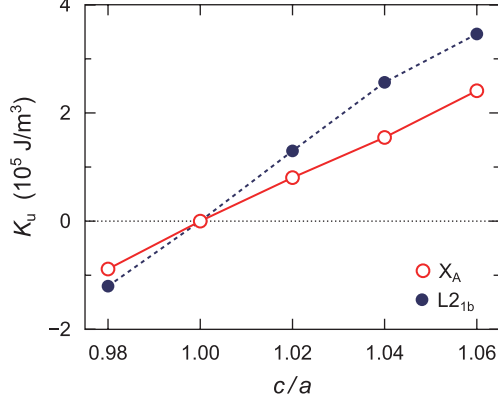


FIG. 13. Axial ratio c/a dependence of uniaxial magnetic anisotropy constant K_u of Mn_2CoGa with the X_A and $L2_{1b}$ phases obtained from first-principles calculation.

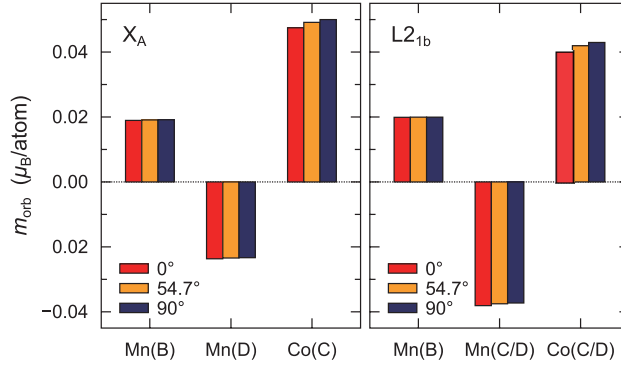


FIG. 14. Calculated orbital magnetic moment m_{orb} of Mn and Co atom in Mn_2CoGa with the X_A and $L2_{1b}$ phases. The angle of 0° , 54.7° , and 90° means the relative angle between magnetization and crystal c -axis.

in both of the X_A and $L2_{1b}$ phases. In figure 15, we depict the density of states (DOS) of X_A - and $L2_{1b}$ - Mn_2CoGa . Figs 15(a) and 15(b) show the total DOS and the local DOS of Mn and Co at C- and/or D-sublattice for the cubic ($c/a = 1.00$) case. Furthermore, Figs. 15(c)–15(f) show the DOS projected into the d -orbitals (d_{xy} , d_{yz} , d_{zx} , $d_{x^2-y^2}$, $d_{3z^2-r^2}$) near the Fermi energy (E_F) for the cubic and tetragonal ($c/a = 1.04$) cases. The degeneracy in t_{2g} (d_{xy} , d_{yz} , d_{zx}) based states and that in e_g ($d_{x^2-y^2}$, $d_{3z^2-r^2}$) based states are removed by the tetragonal distortion. In particular, we can see a significant DOS splitting in $d_{x^2-y^2}$ and $d_{3z^2-r^2}$ states, because $d_{3z^2-r^2}$ ($d_{x^2-y^2}$) orbital spreads to the parallel (perpendicular) direction to the crystal c -axis.

Let us discuss the origin for PMA in tetragonally distorted Mn_2CoGa from the expression

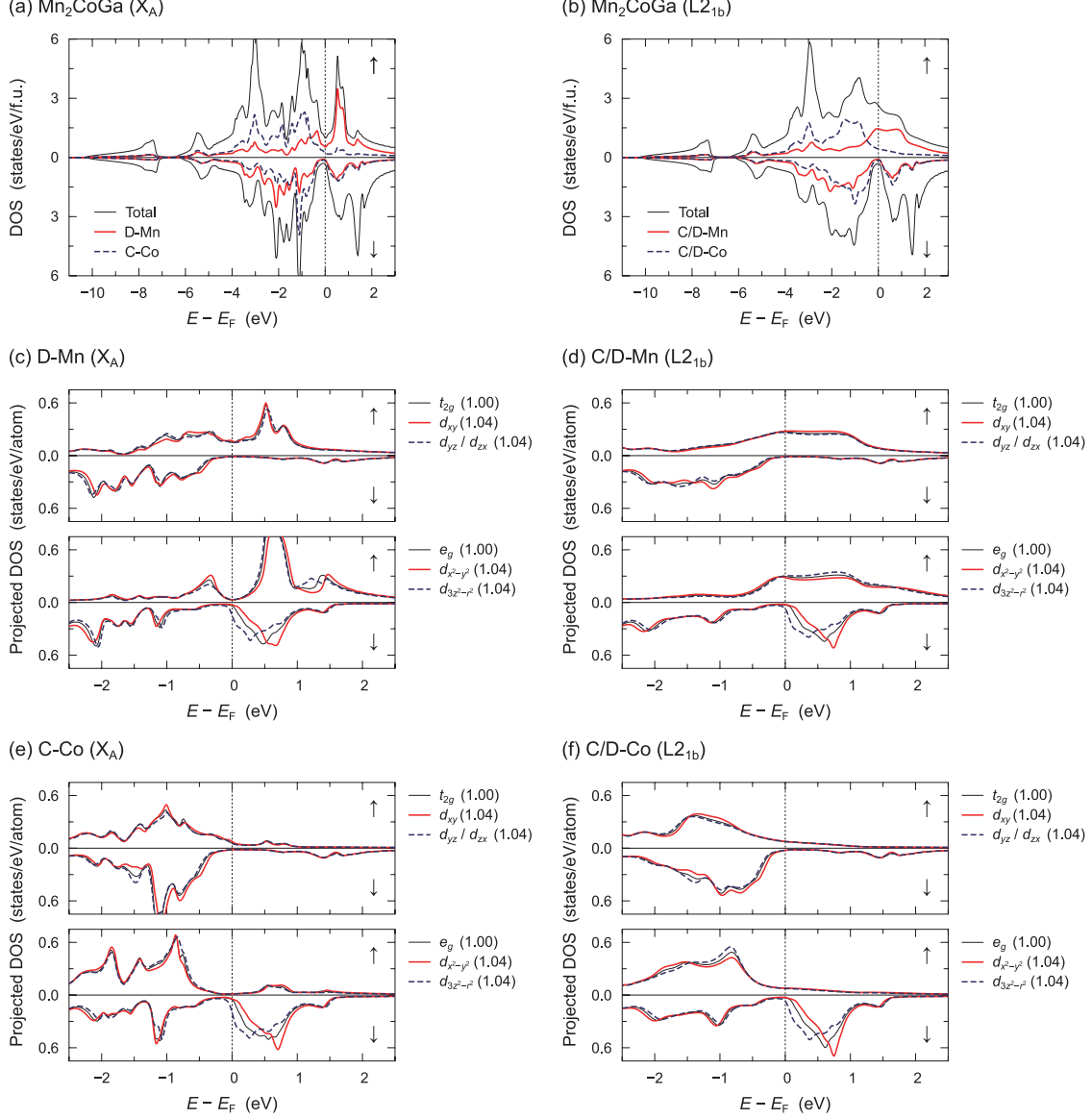


FIG. 15. (a), (b) Total and local DOS of Mn and Co at C- and/or D-sublattice in Mn₂CoGa with the X_A and L2_{1b} phases for $c/a = 1.00$. (c)–(f) Projected DOS into t_{2g} -based d_{xy} , d_{yz} , and d_{zx} orbitals, and into e_g -based $d_{x^2-y^2}$ and $d_{3z^2-r^2}$ orbitals for $c/a = 1.00$ and 1.04 . The values in parenthesis denote c/a . The upper and lower panels of each figure present the DOS of \uparrow - and \downarrow -spin states, respectively.

of Eq. (4) and the projected DOS shown in Figs. 15(c)–15(f). The peaks of $d_{x^2-y^2}^\downarrow$ and $d_{3z^2-r^2}^\downarrow$ states are located just above E_F , and also the d_{yz}^\uparrow state lies below E_F , in Mn and Co at C- and/or D-sublattice with both of the X_A and L2_{1b} phases. These states hybridize each other via spin–orbit coupling, which results in non-zero matrix element of $\langle d_{yz} | \ell_x | d_{x^2-y^2} \rangle$ and

$\langle d_{yz} | \ell_x | d_{3z^2-r^2} \rangle$. In Eq. (4), the mixing of occupied d_{yz}^\uparrow state and unoccupied $d_{x^2-y^2}^\downarrow$ state, and the mixing of occupied d_{yz}^\uparrow state and unoccupied $d_{3z^2-r^2}^\downarrow$ state make for the positive K_u value, *i.e.*, promoting PMA. Note here that $\delta_{\uparrow\downarrow} = 0$ in eq. (4). In Figs. 15(c)–15(f), the peak of the unoccupied $d_{3z^2-r^2}^\downarrow$ state of Mn and Co shifts to lower energy side with increasing c/a ; this enhances the positive contribution of K_u , because the energy difference from the occupied d_{yz}^\uparrow state, $\varepsilon_{u\downarrow} - \varepsilon_{o\uparrow}$, becomes smaller, in Eq. (4). In contrast, the peak of $d_{x^2-y^2}^\downarrow$ shifts to the higher energy side, reducing the positive contribution. We notice that there is a tradeoff relation enhancing and reducing the positive K_u with increasing c/a ; however, the former contribution is three times as large as the latter, because of $|\langle d_{yz} | \ell_x | d_{3z^2-r^2} \rangle|^2 = 3$ and $|\langle d_{yz} | \ell_x | d_{x^2-y^2} \rangle|^2 = 1$. Therefore, the PMA is induced by increasing the positive K_u value in the tetragonally distorted MCG films for $c/a > 1$ through the spin-flip term in Eq. (4), and a qualitative mechanism for the PMA is almost the same regardless of whether crystal structure is the X_A or $L2_{1b}$ phases. On the other hand, the in-plane magnetic anisotropy arises for $c/a < 1$, as shown in Fig. 13, based on the opposite scenario of the above.

V. SUMMARY

Crystal structure and magnetic properties of MCG films on Cr or Ag buffer were investigated experimentally and theoretically. Epitaxial growth of all samples was confirmed using XRD profiles, and the different growth modes were suggested depending on the buffer materials, which possibly caused the different c/a ratios among the samples. Tetragonal distortion of the MCG layers was found for the Cr buffer samples up to the layer thickness of 30 nm, whereas Ag buffer samples exhibited cubic structure which was stable in bulk Mn_2CoGa samples in literature. From magnetization curves measurements, perpendicular magnetization was found in all the Cr buffer samples; on the other hand, all Ag buffer samples exhibited in-plane magnetization. The c/a ratio dependence of K_u clearly exhibited positive correlation, and the maximum value of K_u was 1.6×10^5 J/m³ at room temperature for the 5-nm-thick MCG film on the Cr buffer. Magnetic domain pattern observations using the magneto-optical Kerr microscopy revealed changes of the domain structures depending on the magnitude of K_u . XAS and XMCD spectra were also acquired to elucidate the origin of magnetocrystalline anisotropy in MCG, and unraveled the chemical order of $L2_{1b}$ or X_A phase. In addition, the angular dependence of XMCD spectra revealed that the change of the m_{orb} was negligibly small suggesting a negligible contribution of the spin conserved term,

so called Bruno's term, to K_u . Theoretical values of K_u were evaluated by means of the first principles electronic structure calculation. The positive correlation was also confirmed between the c/a ratios and the values of K_u in the calculation. In addition, the calculated angular dependence of m_{orb} was negligibly small. Those results are consistent with the experimental results. Based on the analysis of the second-order perturbation theory, the origin of the magnetocrystalline anisotropy is proposed that the hybridization between two crystal-field split states with opposite spins, *i.e.*, the spin-flip term near the Fermi level, promotes positive contribution to K_u .

ACKNOWLEDGMENTS

The XAS and XMCD experiments were performed under the Shared Use Program of JAEA Facilities (2018B-E24, and 2019B-E17) with the approval of the Nanotechnology Platform project supported by the Ministry of Education, Culture, Sports, Science and Technology (A-18-AE-0042, and A-19-AE-0037). The synchrotron radiation experiments were performed at the JAEA beam line BL23SU in SPring-8 (2018B3842, and 2019B3844). TK, DT and MM would like to thank Mr. Issei Narita for technical support. This work was partially supported by KAKENHI (JP20K05296) from JSPS, and by a cooperative research program (No.20G0414) of the CRDAM-IMR, Tohoku Univ.

CONFLICT OF INTEREST

The authors have no conflicts to disclose.

DATA AVAILABILITY STATEMENTS

The data that support the findings of this study are available from the corresponding author upon reasonable request.

REFERENCES

- ¹C. Felser and A. Hirohata, eds., *Heusler Alloys* (Springer International Publishing, 2016).
- ²J. Kübler, A. R. William, and C. B. Sommers, *Phys. Rev. B* **28**, 1745 (1983).
- ³S. Ishida, S. Fujii, S. Kashiwagi, and S. Asano, *J. Phys. Soc. Japan* **64**, 2152 (1995).

- ⁴I. Galanakis, P. H. Dederichs, and N. Papanikolaou, *Phys. Rev. B* **66**, 174429 (2002).
- ⁵Y. Miura, K. Nagao, and M. Shirai, *Phys. Rev. B* **69**, 144413 (2004).
- ⁶H. C. Kandpal, G. H. Fecher, C. Felser, and G. Schönhense, *Phys. Rev. B* **73**, 094422 (2006).
- ⁷K. Inomata, S. Okamura, R. Goto, and N. Tezuka, *Jpn. J. Appl. Phys.* **42**, L419 (2003).
- ⁸Y. Sakuraba, J. Nakata, M. Oogane, H. Kubota, Y. Ando, A. Sakuma, and T. Miyazaki, *Jpn. J. Appl. Phys.* **44**, L1100 (2005).
- ⁹J. Schmalhorst, D. Ebke, A. Weddemann, A. Hütten, A. Thomas, G. Reiss, A. Turchanin, A. Götzhäuser, B. Balke, and C. Felser, *J. Appl. Phys.* **104**, 043918 (2008).
- ¹⁰T. Kubota, S. Tsunegi, M. Oogane, S. Mizukami, T. Miyazaki, H. Naganuma, and Y. Ando, *Appl. Phys. Lett.* **94**, 122504 (2009).
- ¹¹M. Yamamoto, T. Ishikawa, T. Taira, G. fang Li, K. ichi Matsuda, and T. Uemura, *J. Phys.: Condens. Matter* **22**, 164212 (2010).
- ¹²H. xi Liu, T. Kawami, K. Moges, T. Uemura, M. Yamamoto, F. Shi, and P. M. Voyles, *J. Phys. D: Appl. Phys.* **48**, 164001 (2015).
- ¹³Y. Sakuraba, M. Ueda, Y. Miura, K. Sato, S. Bosu, K. Saito, M. Shirai, T. J. Konno, and K. Takanashi, *Appl. Phys. Lett.* **101**, 252408 (2012).
- ¹⁴T. Kubota, Z. Wen, and K. Takanashi, *J. Magn. Magn. Mater.* **492**, 165667 (2019).
- ¹⁵K. Miyamoto, K. Iori, A. Kimura, T. Xie, M. Taniguchi, S. Qiao, and K. Tsuchiya, *Solid State Commun.* **128**, 163 (2003).
- ¹⁶N. D. Telling, P. S. Keatley, G. van der Laan, R. J. Hicken, E. Arenholz, Y. Sakuraba, M. Oogane, Y. Ando, and T. Miyazaki, *Phys. Rev. B* **74**, 224439 (2006).
- ¹⁷T. Yoshikawa, V. N. Antonov, T. Kono, M. Kakoki, K. Sumida, K. Miyamoto, Y. Takeda, Y. Saitoh, K. Goto, Y. Sakuraba, K. Hono, A. Ernst, and A. Kimura, *Phys. Rev. B* **102**, 064428 (2020).
- ¹⁸T. Kono, M. Kakoki, T. Yoshikawa, X. Wang, K. Goto, T. Muro, R. Y. Umetsu, and A. Kimura, *Phys. Rev. Lett.* **125**, 216403 (2020).
- ¹⁹M. Kolbe, S. Chadov, E. A. Jorge, G. Schönhense, C. Felser, H.-J. Elmers, M. Kläui, and M. Jourdan, *Phys. Rev. B* **86**, 024422 (2012).
- ²⁰M. Jourdan, J. Minár, J. Braun, A. Kronenberg, S. Chadov, B. Balke, A. Gloskovskii, M. Kolbe, H. Elmers, G. Schönhense, H. Ebert, C. Felser, and M. Kläui, *Nat Commun* **5** (2014), 10.1038/ncomms4974.
- ²¹S. Ishida, S. Asano, and J. Ishida, *J. Phys. Soc. Japan* **53**, 2718 (1984).

- ²²J. Slonczewski, *J. Magn. Magn. Mater.* **159**, L1 (1996).
- ²³S. Ouardi, G. H. Fecher, C. Felser, and J. Kübler, *Phys. Rev. Lett.* **110**, 100401 (2013).
- ²⁴I. Galanakis, K. Özdoğan, E. Şaşıoğlu, and S. Blügel, *J. Appl. Phys.* **115**, 093908 (2014).
- ²⁵Y. Xin, H. Hao, Y. Ma, H. Luo, F. Meng, H. Liu, E. Liu, and G. Wu, *Intermetallics* **80**, 10 (2017).
- ²⁶V. Alijani, J. Winterlik, G. H. Fecher, and C. Felser, *Appl. Phys. Lett.* **99**, 222510 (2011).
- ²⁷P. Klaer, B. Balke, V. Alijani, J. Winterlik, G. H. Fecher, C. Felser, and H. J. Elmers, *Phys. Rev. B* **84**, 144413 (2011).
- ²⁸S. Chadov, J. Kiss, and C. Felser, *Adv. Funct. Mater.* **23**, 832 (2012).
- ²⁹S. Ouardi, T. Kubota, G. H. Fecher, R. Stinshoff, S. Mizukami, T. Miyazaki, E. Ikenaga, and C. Felser, *Appl. Phys. Lett.* **101**, 242406 (2012).
- ³⁰T. Kubota, S. Ouardi, S. Mizukami, G. H. Fecher, C. Felser, Y. Ando, and T. Miyazaki, *J. Appl. Phys.* **113**, 17C723 (2013).
- ³¹T. Kubota, S. Mizukami, Q. L. Ma, H. Naganuma, M. Oogane, Y. Ando, and T. Miyazaki, *J. Appl. Phys.* **115**, 17C704 (2014).
- ³²Y. Wang, J. Zhang, X.-G. Zhang, H.-P. Cheng, and X. F. Han, *Phys. Rev. B* **82**, 054405 (2010).
- ³³Z. Wen, H. Sukegawa, S. Mitani, and K. Inomata, *Appl. Phys. Lett.* **98**, 242507 (2011).
- ³⁴T. Kamada, T. Kubota, S. Takahashi, Y. Sonobe, and K. Takanashi, *IEEE Trans. Magn.* **50**, 2600304 (2014).
- ³⁵T. Kubota, Y. Ina, M. Tsujikawa, S. Morikawa, H. Narisawa, Z. Wen, M. Shirai, and K. Takanashi, *J. Phys. D: Appl. Phys.* **50**, 014004 (2016).
- ³⁶K. Nagai, H. Fujiwara, H. Aratani, S. Fujioka, H. Yomosa, Y. Nakatani, T. Kiss, A. Sekiyama, F. Kuroda, H. Fujii, T. Oguchi, A. Tanaka, J. Miyawaki, Y. Harada, Y. Takeda, Y. Saitoh, S. Suga, and R. Y. Umetsu, *Phys. Rev. B* **97**, 035143 (2018).
- ³⁷M. Meinert, J.-M. Schmalhorst, C. Klewe, G. Reiss, E. Arenholz, T. Böhnert, and K. Nielsch, *Phys. Rev. B* **84**, 132405 (2011).
- ³⁸S. Ouardi, G. H. Fecher, T. Kubota, S. Mizukami, E. Ikenaga, T. Nakamura, and C. Felser, *J. Phys. D: Appl. Phys.* **48**, 164007 (2015).
- ³⁹Y. Saitoh, Y. Fukuda, Y. Takeda, H. Yamagami, S. Takahashi, Y. Asano, T. Hara, K. Shirasawa, M. Takeuchi, T. Tanaka, and H. Kitamura, *J. Synchrotron Radiat.* **19**, 388 (2012).
- ⁴⁰E. Bauer, *Appl. Surf. Sci.* **11-12**, 479 (1982).
- ⁴¹M. T. Kief and W. F. Egelhoff, *Phys. Rev. B* **47**, 10785 (1993).

- ⁴²J. H. V. D. Merwe, *J. Appl. Phys.* **34**, 117 (1963).
- ⁴³J. H. V. D. Merwe, *J. Appl. Phys.* **34**, 123 (1963).
- ⁴⁴N. H. Fletcher, *J. Appl. Phys.* **35**, 234 (1964).
- ⁴⁵L. Z. Mezey and J. Giber, *Jpn. J. Appl. Phys.* **21**, 1569 (1982).
- ⁴⁶G. Guisbiers and M. José-Yacaman, in *Encyclopedia of Interfacial Chemistry* (Elsevier, 2018) pp. 875–885.
- ⁴⁷L. Vitos, A. Ruban, H. Skriver, and J. Kollár, *Surf. Sci.* **411**, 186 (1998).
- ⁴⁸R. Y. Umetsu, M. Tsujikawa, K. Saito, K. Ono, T. Ishigaki, R. Kainuma, and M. Shirai, *J. Phys.: Condens. Matter* **31**, 065801 (2018).
- ⁴⁹The calculation details for the magnetic moments with the offstoichiometry and the disorder are described in section ?? of Supplementary Material.
- ⁵⁰R. Belhi, A. Fassatoui, A. A. Adjanoh, and K. Abdelmoula, *J. Appl. Phys.* **116**, 013908 (2014).
- ⁵¹S. Mallick, S. S. Mishra, and S. Bedanta, *Sci. Rep.* **8**, 11648 (2018).
- ⁵²R. S. Alex Hubert, “Magnetic domains,” (Springer-Verlag GmbH, 1998) pp. pp107–354.
- ⁵³B. T. Thole, P. Carra, F. Sette, and G. van der Laan, *Phys. Rev. Lett.* **68**, 1943 (1992).
- ⁵⁴P. Carra, B. T. Thole, M. Altarelli, and X. Wang, *Phys. Rev. Lett.* **70**, 694 (1993).
- ⁵⁵J. Stöhr and H. König, *Phys. Rev. Lett.* **75**, 3748 (1995).
- ⁵⁶G. van der Laan and A. I. Figueroa, *Coord. Chem. Rev.* **277-278**, 95 (2014).
- ⁵⁷T. Koide, H. Miyauchi, J. Okamoto, T. Shidara, A. Fujimori, H. Fukutani, K. Amemiya, H. Takeshita, S. Yuasa, T. Katayama, and Y. Suzuki, *Phys. Rev. Lett.* **87**, 257201 (2001).
- ⁵⁸K. Edmonds, G. van der Laan, and G. Panaccione, *Semicond Sci. Technol.* **30**, 043001 (2015).
- ⁵⁹Y. Teramura, A. Tanaka, and T. Jo, *J. Phys. Soc. Japan* **65**, 1053 (1996).
- ⁶⁰H. A. Dürr, G. van der Laan, D. Spanke, F. U. Hillebrecht, and N. B. Brookes, *Phys. Rev. B* **56**, 8156 (1997).
- ⁶¹E. Goering, *Philos. Mag.* **85**, 2895 (2005).
- ⁶²The values of n_h are averages of four calculated values. In the calculation, n_{3d} obtained by the first principles calculations was used, and $n_h = 10 - n_{3d}$ was assumed. The for cases were Mn_2CoGa with X_A and $L2_{1b}$ phases and c/a ratios of 1.00 and 1.04.
- ⁶³D. Weller, J. Stöhr, R. Nakajima, A. Carl, M. G. Samant, C. Chappert, R. Mégy, P. Beauvillain, P. Veillet, and G. A. Held, *Phys. Rev. Lett.* **75**, 3752 (1995).
- ⁶⁴P. Bruno, *Phys. Rev. B* **39**, 865 (1989).

- ⁶⁵G. van der Laan, *J. Phys.: Condens. Matter* **10**, 3239 (1998).
- ⁶⁶Y. Kota and A. Sakuma, *J. Phys. Soc. Jpn.* **83**, 034715 (2014).
- ⁶⁷T. Kubota, K. Kodama, T. Nakamura, Y. Sakuraba, M. Oogane, K. Takanashi, and Y. Ando, *Appl. Phys. Lett.* **95**, 222503 (2009).
- ⁶⁸J. Karel, F. Bernardi, C. Wang, R. Stinshoff, N.-O. Born, S. Ouardi, U. Burkhardt, G. H. Fecher, and C. Felser, *Phys. Chem. Chem. Phys.* **17**, 31707 (2015).
- ⁶⁹K. Minakuchi, R. Umetsu, K. Kobayashi, M. Nagasako, and R. Kainuma, *J. Alloys* **645**, 577 (2015).
- ⁷⁰I. Turek, V. Drchal, J. Kudrnovský, M. Sob, I. Turek, and P. Weinberger, *Electronic Structure of Disordered Alloys, Surfaces and Interfaces* (Springer US, 1996).
- ⁷¹I. Turek, V. Drchal, and J. Kudrnovský, *Philos. Mag.* **88**, 2787 (2008).
- ⁷²Y. Kota and A. Sakuma, *J. Appl. Phys.* **111**, 07A310 (2012).
- ⁷³Y. Kota and A. Sakuma, *J. Phys. Soc. Japan* **81**, 084705 (2012).
- ⁷⁴J. Okabayashi, Y. Miura, Y. Kota, K. Z. Suzuki, A. Sakuma, and S. Mizukami, *Sci. Rep.* **10**, 9744 (2020).
- ⁷⁵I. V. Solovyev, P. H. Dederichs, and I. Mertig, *Phys. Rev. B* **52**, 13419 (1995).
- ⁷⁶L. Ke, *Phys. Rev. B* **99**, 054418 (2019).